RSC Advances

ROYAL SOCIETY OF CHEMISTRY

PAPER

View Article Online
View Journal | View Issue

Check for updates

Cite this: *RSC Adv.*, 2024, **14**, 12464

Influence of potassium doping on the structural, conduction mechanism, and dielectric properties of $CaFe_2O_4$

Mohamed Mounir Bouzayani, [a] Manel Ben Abdessalem, *[a] Ibtihel Soudani, [a] Abderrazek Oueslati [b] and Abdelhedi Aydi [a]

Received 10th January 2024
Accepted 11th April 2024

DOI: 10.1039/d4ra00260a

rsc.li/rsc-advances

The frequency and temperature-related dielectric relaxation and electrical conduction mechanisms in potassium-doped $CaFe_2O_4$ oxide ceramic were investigated in this study throughout a temperature range of 313–673 K. The synthesis of the $KCaFe_2O_4$ compound was accomplished through a solid-state reaction route. The X-ray diffraction pattern at room temperature confirmed that the ceramic $KCaFe_2O_4$ crystallizes in the orthorhombic system with the *Pbnm* space group. The EDX analysis proved the absence of external elements. The surface morphology of the samples was examined using scanning electron microscopy. The conduction mechanism, validated as CBH conduction, was examined using the temperature-dependent variation of Jonscher's power law exponent. Using Nyquist plots, we have effectively constructed a relevant equivalent circuit that encompasses the influences originating from both the grains and the grain boundaries. Furthermore, in $KCaFe_2O_4$, the induced dielectric relaxation from the non-Debye to Debye type model is demonstrated by the thermal analysis of $M''(\omega)$ and $-Z''(\omega)$ as a function of frequency.

1. Introduction

Since the publication of its crystal structure, extensive research has been dedicated to calcium ferrite ($CaFe_2O_4$ or CFO) due to its captivating structural, electrical, magnetic, and chemical properties.[1] Its multifaceted applications include its incorporation into electronic devices,[2] its role as a catalyst in diverse reactions,[3,4] its function as a photocathode facilitating the hydrogen evolution reaction in water splitting,[5,6] its use as a ceramic pigment and coating,[7] and its application as electrodes in solid oxide fuel cells.[8] The unique crystal structure of CFO differs from the majority of recognized ferrites.

Unlike the typical cubic spinel shape found in many ferrites, CFO exhibits a unit cell deviation, leading to an orthorhombic crystal structure. This difference is attributed to the ionic radius of Ca^{2+} ($Ca^{2+} = 1.35$ Å), which is larger than that of Fe^{3+} ($Fe^{3+} = 0.645$ Å).This difference prevents it from incorporating into the tetrahedral sites of a cubic oxygen lattice at the central characteristic faces of a spinel.[9] The characteristics of the lattice can be tailored to meet specific needs by introducing divalent and trivalent metal ions. By substituting atoms in the A and B sites, the cationic distribution of ferrites undergoes modification. Transition metal cations, including Zn[10] and Ti,[11] can be integrated across a wide range of applications.

Owing to its distinctive structure, CFO serves as a prototype for other crystals. Bulk CFO has been employed as anode electrodes in Li-ion batteries,[12] pigments,[13] and photocathode materials.[14] Intensive investigation has been carried out regarding bulk CFO structure, thermodynamic properties, and magnetic characteristics.[15] Electronic structure simulations were performed to gain insights into its optical properties.[16] Mössbauer spectra and neutron diffraction profiles of CFO indicate the antiferromagnetic ordering of Fe atoms in two octahedral sites, Fe_1 and Fe_2, occurring below the Néel temperature of 180 K.[17]

Consequently, the CFO readily adopts an off-spinel structure during formation and crystallization. Hence, exploring the dielectric properties of CFO becomes intriguing, offering insights into its suitability for diverse applications.[18,19]

Potassium ions (K^+) were introduced into the base structure of ferrite owing to their high reactivity and distinctive physicochemical characteristics, facilitating their seamless integration. Alkaline metals are very reactive, releasing a single electron on the last layer to other metals in the ferrite composition.[20] Incorporating metal cations into the ferrite structure can notably enhance the conduction mechanism, optical characteristics, or magnetic properties of semiconductors.[21–23]

In the current investigation, the focus was on exploring the characteristics of K-doped $CaFe_2O_4$ ($KCaFe_2O_4$) mixed ferrite. On the octahedral B site, K^+ ($r(k^+) = 1.60$ Å) has a significantly higher ionic radius compared with that of Ca^{2+} ($r(Ca^{2+}) = 1.35$ Å).[24]

---

[a] *Laboratory of Multifunctional Materials and Applications (LaMMA), LR16ES18, Faculty of Sciences, University of Sfax, B. P. 1171, 3000 Sfax, Tunisia. E-mail: medmounirbz16@gmail.com*

[b] *Laboratory of Spectroscopic Characterization and Optical Materials (laSCOM), Faculty of Sciences, University of Sfax, B. P. 1171, 3000 Sfax, Tunisia*

The substitution of the K^+ ion in place of the Ca^{2+} ion can lead to alterations in the geometry of the crystals, thus influencing the dielectric properties of these materials, which are due to the difference in the ionic radii. Recently, several research teams have made significant efforts in the synthesis and characterization of various ferrite materials $CaFe_2O_4$,[25,26] $Ni_{0.6}Zn_{0.4}Al_{0.5}Fe_{1.5}O_4$,[27] $LiMnFe_2O_4$ (ref. 28 and 29) and $K_xMg_{1-x}Fe_2O_4$.[30] Despite the extensive research conducted on calcium ferrites, there is a notable lack of attention to the impact of potassium doping on the properties of these materials.

As part of this effort, we synthesized $KCaFe_2O_4$ (KCFO) ferrite samples using the solid-state method and investigated their structural and dielectric characteristics. The structural analysis was performed under (RT) conditions, while the investigation into the dielectric properties involved employing impedance spectroscopy at different frequencies and temperatures. To maintain brevity, the synthesized KCFO sample is consistently denoted as KCFO throughout this manuscript.

2. Material and method

We used a conventional solid-state reaction to synthesize the KCFO compound. K_2CO_3 (Sigma-Aldrich, 99%), $CaCO_3$ (Sigma-Aldrich, 99%), and Fe_2O_3 (Sigma-Aldrich, 99%) were mixed in proportional ratios. The obtained powder was submitted to a first thermal treatment at 700 K for 10 hours (h) to release the CO_2 gas. Then, we verified the gas emissions by checking the weight. Finally, the sintering process was at 950 K for 6 h.

The purity of the sample was determined by X-ray diffraction on powder by "D8 ADVANCE, Bruker" at room temperature (RT) with Cu Kα ($\lambda = 1.5406$ Å) radiation in the angle range of $5° < 2\theta < 80°$ and a speed of scan of 20 min^{-1} counting time for each 0.02° in step.

Furthermore, the morphological characterization was performed using a scanning electron microscope (SEM) (Bruker Nano GmbH Berlin, Germany), to estimate the particle sizes.

Additionally, Raman spectra were obtained at RT, in the range of 100–1100 cm^{-1}, using a SENTERRA spectrometer (Bruker), with excitation at 540 nm. FTIR spectra were acquired using a Bruker Tensor 27 spectrophotometer.

Electric measurements were conducted on a pellet measuring 8 mm in diameter and 1 mm in thickness. Complex impedance spectroscopy was employed using the "Solartron 1260" over a frequency range of 10–10^6 Hz at different temperatures. The pellets, featuring a thin layer of silver coating on opposite surfaces, were placed between two copper electrodes in a specially designed holder to ensure optimal contact.

3. Results and discussion

3.1. Structural and morphological studies

X-ray diffraction (XRD) is applicable for assessing the purity of a synthesized substance. Fig. 1 shows the XRD pattern of KCFO. Lattice parameters were determined using a global profile-matching method with Fullprof software.[31] This indicates that the KCFO sample crystallizes in an orthorhombic system with a *Pbnm* space group.

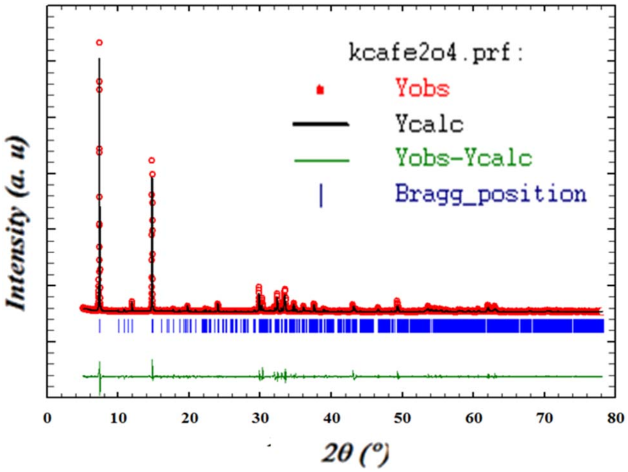

Fig. 1 The Rietveld refinement XRD of synthesized of KCFO at room temperature.

Table 1 Rietveld refined parameters for $KCa_{0.5}Fe_2O_4$

Compounds	$KCa_{0.5}Fe_2O_4$ (room temperature)
System	Orthorhombic
Space group	*Pbnm*
Lattice parameters	
a	17.609 Å
b	16.287 Å
c	5.499 Å
$\alpha = \beta = \gamma$	90°
Z	4
Reliability factors	
RP/RwP/Rexp	35.8%/36.9%/19.89%
χ^2	3.44

The unit cell parameters are gathered in Table 1. These values are higher than those given in the literature, which is attributed to the larger K^+ ionic radius compared to Ca^{2+}.[32–34]

The average size of crystallites (DSC = 140.07 nm) is calculated through the classical Debye–Scherrer equation,[28] employing the full width at half maximum.

$$\beta \cos \theta D_{sc} = k\lambda \quad (1)$$

Here, β represents the half-width measured for the intense diffraction peak corresponding to the plane (*hkl*), θ denotes the diffraction Bragg angle for the most intense peak in radians, D_{sc} stands for the crystallite size, K is the shape factor with an approximate value of 0.9, and λ represents the wavelength of the X-ray used. The observed crystallite size of KCFO is approximately 140.07 nm, confirming the nanoscale dimensions of our ferrite sample.

3.2. SEM and EDX analysis

To evaluate the sample morphology and particle size, a scanning electron microscope (SEM) is used. The SEM image of the examined material is summarized in Fig. 2(a). The micrograph

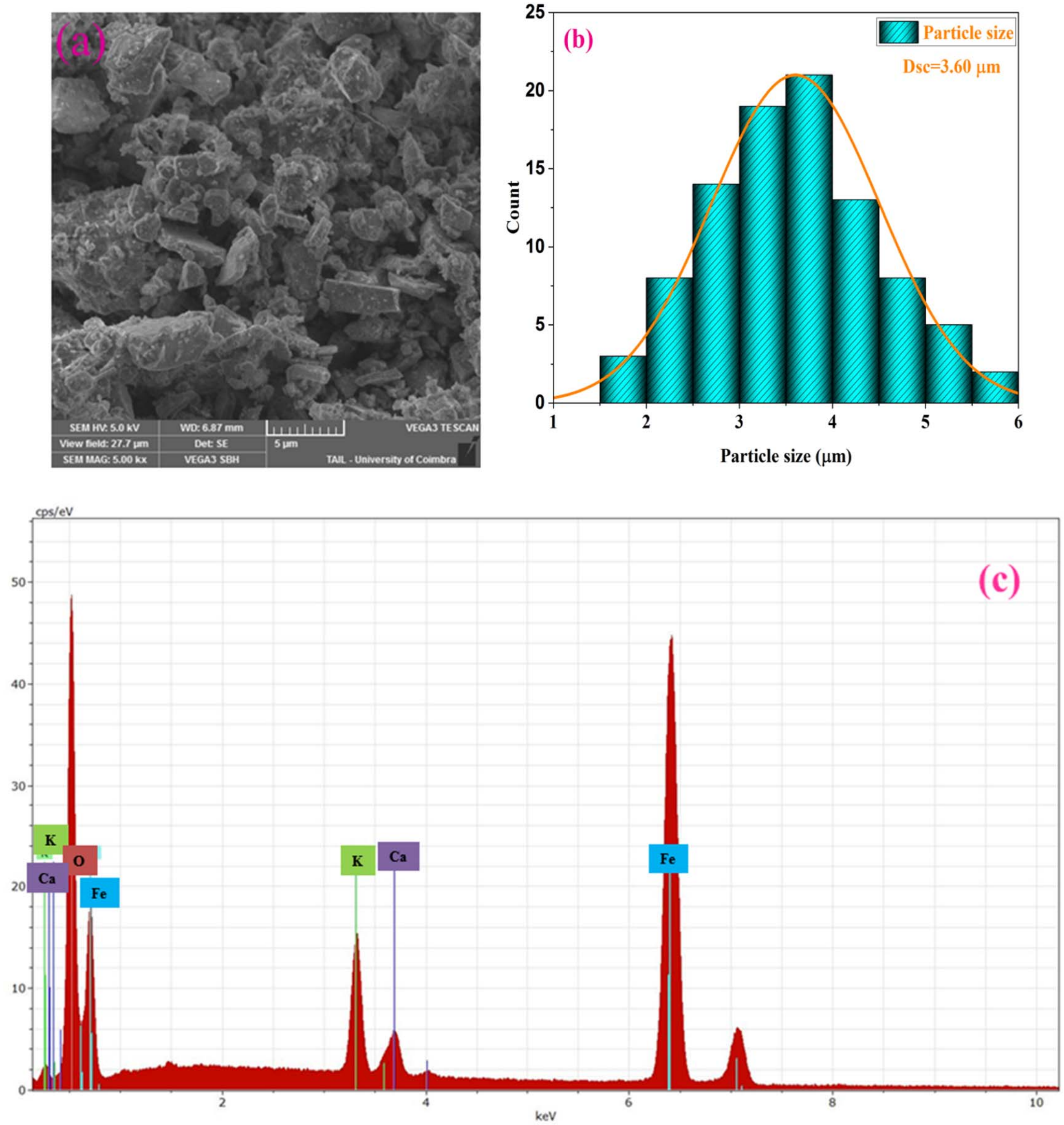

Fig. 2 (a) scanning electron microscopy images, (b) distribution histogram of grains and (c) EDX spectrum of the compound KCFO.

shows the aggregation of the main particles and a Lorentzian fit using the image analyzer software Image J, which predicts an average particle size of 3.60 μm (Fig. 2(b)).This indicates that the grains possess a polycrystalline structure, as evidenced by the relatively small crystallite size determined from the XRD analysis.

The chemical properties of the synthesized compound were examined by energy-dispersive X-ray spectroscopy (EDX). The elemental analysis of the KCFO sample at RT using EDX is shown in Fig. 2(c), and the spectra support the existence of all the constituent elements of KCFO, such as K, Ca, Fe, and O. This provides proof that no embedded parts have been lost or contaminated.

3.3. Raman and infrared spectroscopy analysis

The FTIR spectroscopy technique is useful for determining chemical absorption. The ferrite spinel's metal oxygen is assigned to two broad bands in the spectrum (Fig. 3). The highest ν_1 band in the range 800–600 cm^{-1} corresponds to tetrahedral metal stretching vibrations (Td), while the lowest two bands in the range 550–400 cm^{-1} are assigned to the octahedral stretching of the metal (Oh).[35]

Fig. 4 shows the Raman spectra of KCFO ceramic measured at RT. Deconvolution of the raman spectrum of KCFO using LabSpec5 software using the pseudo-Voigt function shows the presence of twelve vibration modes. These modes were observed at 116.8, 158.7, 178.0, 279.9, 329.0, 370.2, 472.5, 499.7, 528.9, 609.6, 675.4, and 721.8 cm^{-1}. Using irreducible representations, the Raman active modes in the orthorhombic phase with the *Pbnm* space group can be written as follows:$\Gamma = 3A_g + 3B_{1g} + 3B_{2g} + 3B_{3g}$.[36]

The peaks at 116.8, 158.7, 178.0, 279.9, and 472.5 cm^{-1} were attributed to the Fe–O–Ca bonds; which correspond to the A_g, B_{2g}, A_g, A_g, and B_{2g} optical modes, respectively. Hence, oxygen

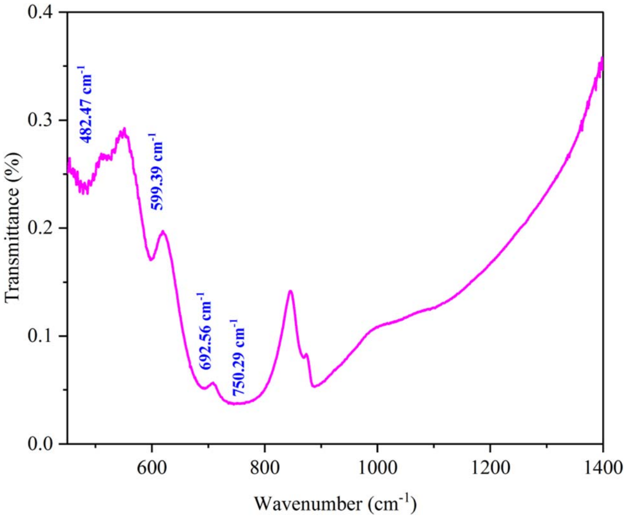

Fig. 3 FTIR spectrum of KCFO.

octahedral modes were between 329 and 370.2 cm^{-1}, oxygen octahedral bending vibration (B. V.) ranged between 472.5 and 499.7 (B_{2g}) cm^{-1}, and oxygen stretching vibrations were above 528.9 cm^{-1} (S. V.).[37] Raman peaks at 499.7, 528.9, 609.6, 675.4, and 721.8 cm^{-1} may be due to the stretching and bending of O–Fe–O.[38]

4. Impedance spectroscopy

4.1. Dielectric measurements

The dielectric permittivity offers crucial insights into the characteristics of the material being produced. It signifies the material's capacity to polarize when subjected to an applied electric field.[39] The dielectric response of any material is given by the complex dielectric constant:

$$\varepsilon^* = \varepsilon' - j\varepsilon'' = \frac{1}{j\omega C_0 Z^*} \tag{2}$$

ε' denotes the real component of the dielectric permittivity, reflecting the stored energy, while ε'' represents the imaginary component, which characterizes the dissipation energy within the material. C_0 denotes the vacuum capacitance and ω is the angular frequency ($\omega = 2\pi f$).

Furthermore, the dielectric loss factor is defined as the ratio of the imaginary part (ε'') and real part (ε') of the complex permittivity (ε^*)

$$\tan\delta = \frac{\varepsilon'}{\varepsilon''} \tag{3}$$

The investigation involves analyzing the variation of ε' (ω) and tan δ with frequency across the temperature range of 313–673 K.

In Fig. 5(a), the frequency-dependent ε' values are depicted across various temperatures.

The generated materials showed higher ε' values at low frequencies, suggesting that they could be viable options for low-frequency energy storage.[40] Similarly, the ε' values fall as the frequency rises, which leads to a decrease in energy storage capacity.[41] Furthermore, the dielectric constant values rise as the temperature increases at a certain frequency. The thermal activation of charge carriers, which affects polarization, is specified by this nature. Ionic, electronic, orientational, and interfacial polarization are the four primary categories. The relaxation components of polarizability in the system involve orientation and interfacial polarizations, while the resonance components encompass ionic and electronic polarizations.[42]

Conversely, it was imperative to explore the materials intended for optoelectronic applications concerning the "dissipation factor," illustrated as tan(δ) in Fig. 5(b). Here, δ is defined mathematically as the angle between the voltage and charging current, commonly referred to as the "loss angle".[43] The primary cause of dielectric loss stems from various physical phenomena, including the conduction process, dielectric relaxation, molecular dipole moment, and interfacial polarization.[44] At lower frequencies, additional energy is needed to

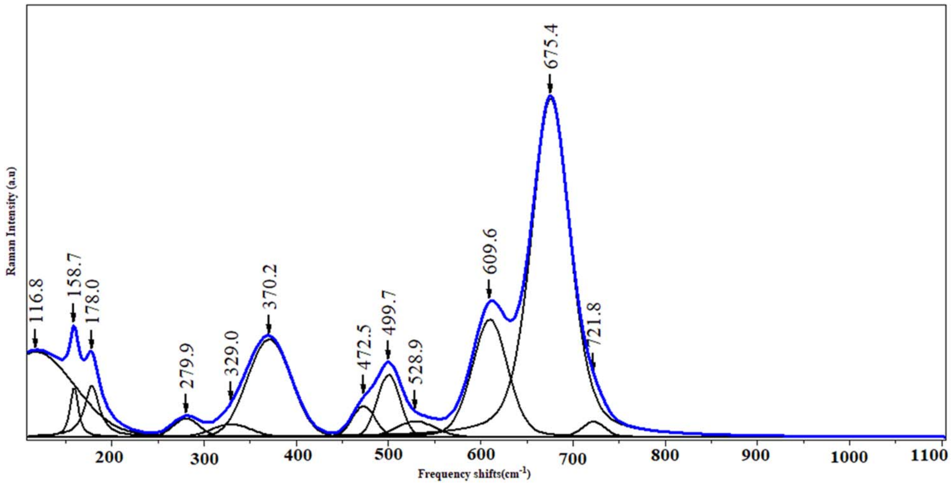

Fig. 4 Raman spectra of the KCFO ceramic at room temperature.

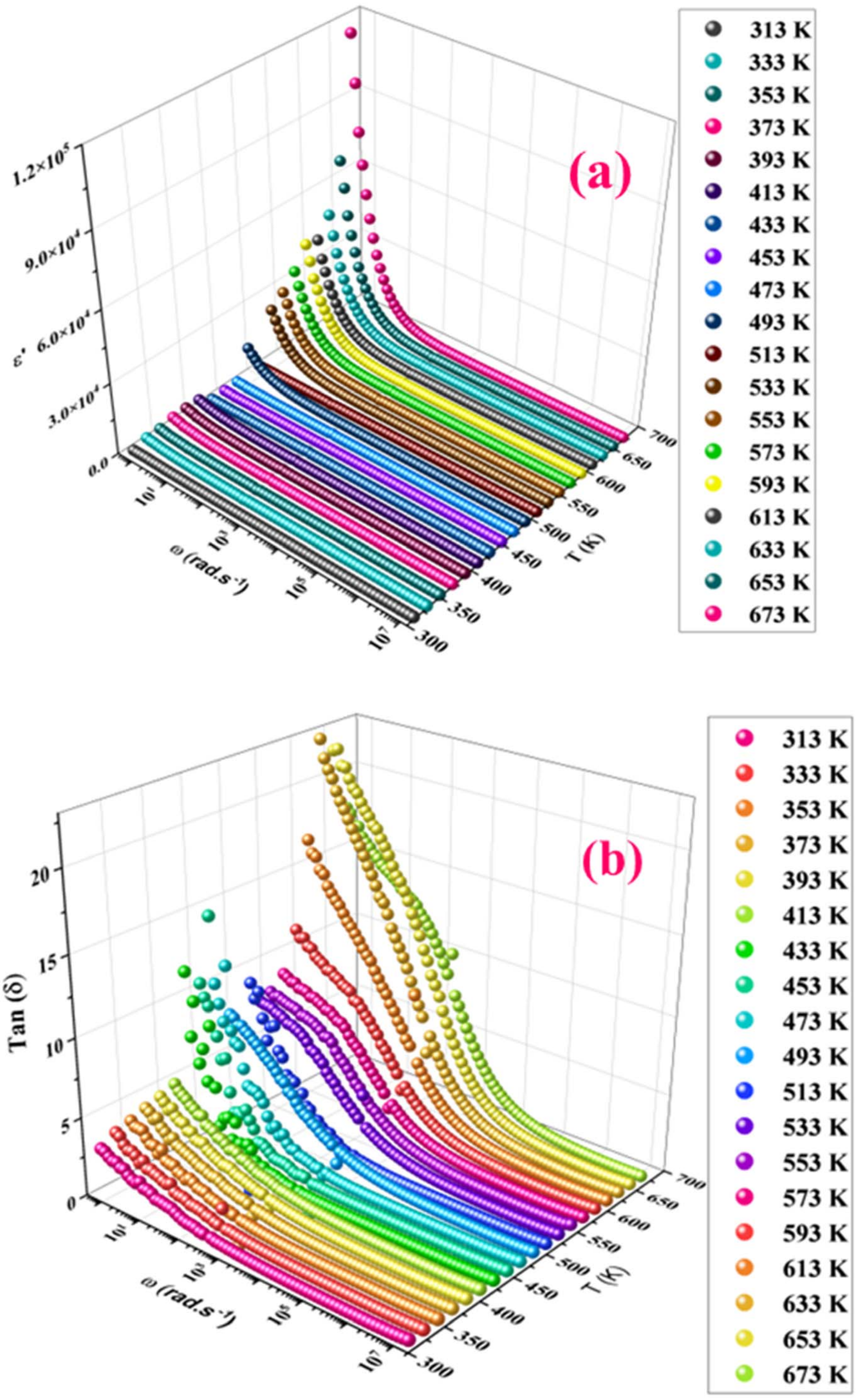

Fig. 5 (a) Dielectric constants (ε') of KCFO nanoparticles pellet at different Temperature. (b) Frequency-dependent dielectric loss of KCFO ceramic measured at various temperatures.

induce the movement of charge carriers. Consequently, tan(δ) values tend to be higher within this frequency range.[45] As the frequency increases, the resistivity of the material decreases, resulting in a more efficient movement of charge carriers that necessitates less energy. As a result, the dielectric loss diminishes in the high-frequency range. This presents opportunities for exploring these materials for potential applications in electrical devices.[46]

It also indicates that increased temperatures and reduced frequencies lead to greater dielectric loss, clearly indicating a rise in the material's conductivity.[47]

Fig. 6(a) illustrates the temperature dependency of the real component (ε') of the complex electric permittivity across various frequencies. The ε' shows a significant dielectric peak of about 413 K, which can be the Ferro-Paraelectric (FP) type phase transition. Since KCFO has been identified as a ferroelectric material in prior studies, this prompts the necessity to investigate whether it exhibits classic ferroelectric behavior or relaxor characteristics. Fig. 6(a) shows that the FP transition temperature ($T_C = 413$ K) is frequency independent, which proves that KCFO is a classic ferroelectric.[48,49]

Fig. 6(b) depicts the plot of Curie–Weiss ($1/\varepsilon'_r$) as a function of temperature at a constant frequency of 500 Hz. The plot exhibits a straight line just above the temperature of the phase transition.

To further study the phase transition behavior of the KCFO sample, we estimated the diffusion parameter using an empirical formula developed by Uchino *et al.*:[50,51]

$$\frac{1}{\varepsilon'_r} - \frac{1}{\varepsilon'_{\max}} = \frac{(T - T_m)^\gamma}{C} \quad T > T_m \tag{4}$$

where T_m is the maximum value at Curie–Weiss temperature T, $\varepsilon'_{\max}$ is the dielectric constant C is the Curie constant and γ is the degree of diffuseness.

In general, the value of γ between these limits ($1 < \gamma < 2$) provide an incomplete diffuse phase transition. According Uchino *et al.*, for a classical transition γ approximate to 1, while an ideal relaxor ferroelectric ones approximate to 2.[52] In our study, the γ values determined for different frequencies were found to be close to unity. Consequently, we can infer that the KCFO compound exhibits classical ferroelectric behavior.

4.2. AC conductivity

In Fig. 7(a), we observe the changes in AC conductivity with respect to frequency over a temperature range spanning from 313 K to 673 K. The DC conductivity is ascribed to the conductivity measured in the low-frequency region, which remains largely unaffected by changes in frequency. At high frequencies, however, the conductivity exhibits a frequency dispersion that is mostly due to AC conductivity. At low frequencies, activated hopping causes random diffusion of charge carriers, resulting in dc conductivity (σ_{dc}). Ions exhibit a coordinated back-and-forth motion in the frequency dispersive region. The jump relaxation model suggested by Funke and Hoppe[52] can explain this frequency-independent DC and

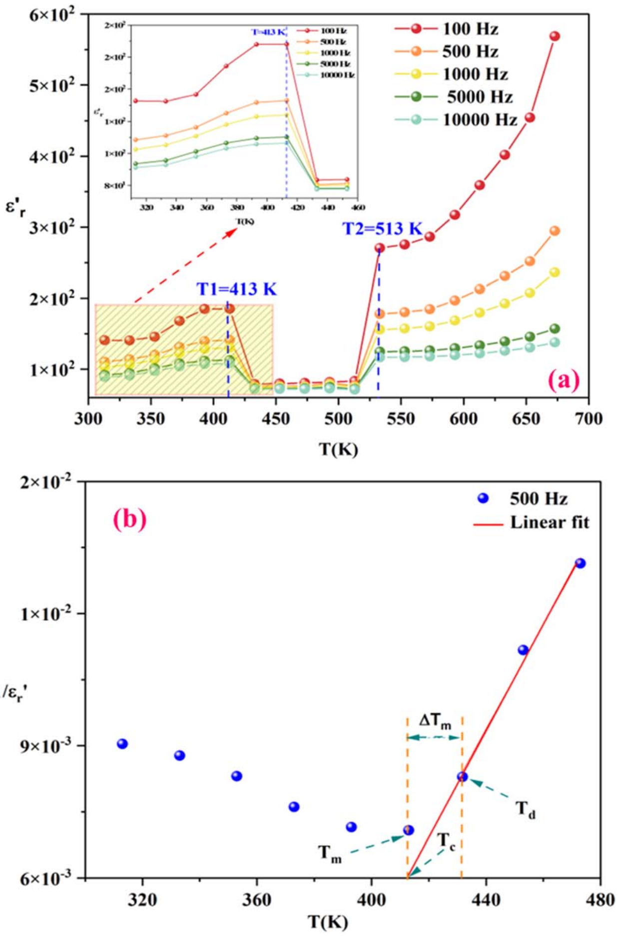

Fig. 6 (a) Shows the temperature dependence of the real ε' parts *vs.* temperature at selected frequencies. (b) The inverse of dielectric constant ($1/\varepsilon'_r$) as a function of temperature of the compound KCFO.

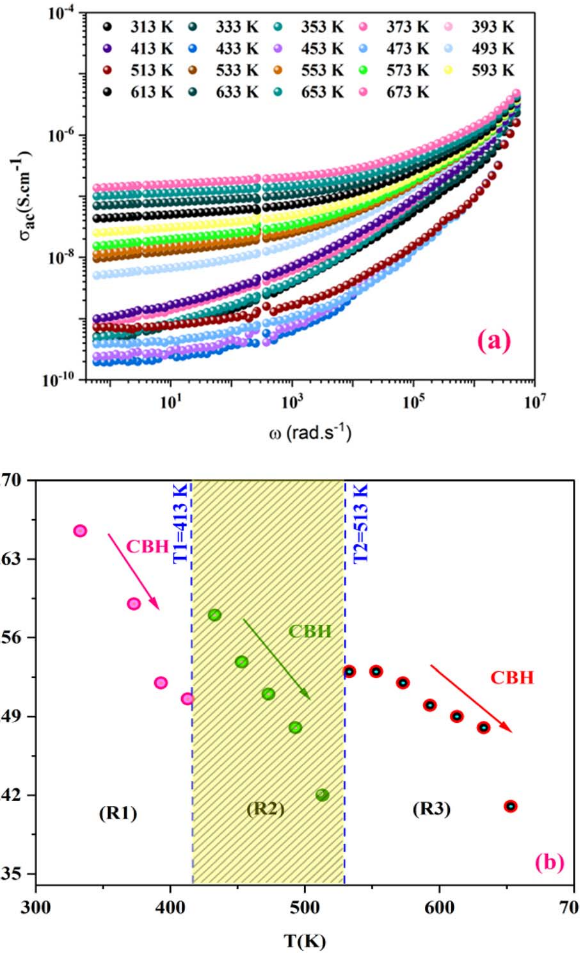

Fig. 7 (a) Frequency dependency of conductivity, (b) temperature dependence of the exponent "s" of KCFO sample prepared with the solid−states method.

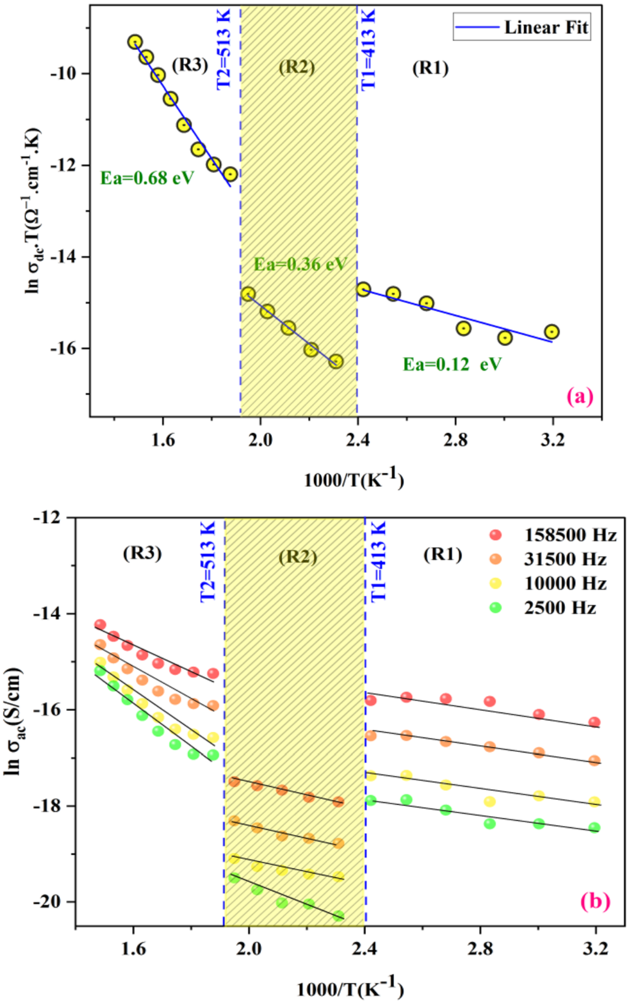

Fig. 8 (a) Arrhenius fits of σ_{dc} (b) evolution of ln ($\sigma_{ac}T$) as a function of (1000/T).

frequency-dependent alternating conductivity. At low frequencies, conductivity primarily arises from successful hops, facilitating long-distance ionic translational motion. The ratio of successful hopping to failed hopping governs the dispersion observed in the conductivity spectra. In the high-frequency regime, there are more failed hops, leading to increased dispersion.

The AC conductivity curve is fitted using the Jonscher power law:[53,54]

$$\sigma_{ac}(\omega) = \sigma_{dc} + \sigma(\omega) = \sigma_{dc} + A\omega^{s} \tag{5}$$

Here, σ_{dc} denotes the DC conductivity of the material; A denotes the pre-exponential factor, ω represents the angular frequency, and s stands for the power-law exponent. The power-law exponent s reflects how the mobile ions interact with their surrounding lattices, with s typically falling within the range of 0 to 1.[53] This can encompass various physical processes such as quantum mechanical tunneling (QMT),[55] non-overlapping small polaron tunneling (NSPT),[56] correlated barrier hopping (CBH),[57,58] and overlapping large-polaron tunneling (OLPT).[59] As shown in Fig. 7(b), the variation of the exponent's as a function of temperature in the range from 313 to 673 K's decreases with the increase in temperature, this suggests that the CBH model serves as an appropriate framework for characterizing the conduction mechanism in the compound under investigation.

Table 2 The activation energy values at chosen frequencies

Frequency (Hz)		2500	10 000	31 500	158 500
E_a (meV)	Region (I)	71 meV	66 meV	58 meV	51 meV
	Region (II)	175 meV	108 meV	105 meV	101 meV
	Region (III)	461 meV	350 meV	283 meV	224 mev

σ_{dc} is determined from fitting the Jonscher power law across all temperatures and is observed to adhere to the Arrhenius relationship:

$$\sigma_{dc} = \sigma_0 \exp\left(-\frac{E_a}{K_B T}\right) \tag{6}$$

Here σ_0 is the preexponential factor, E_a represents the activation energy, k_B is the Boltzmann constant, and T is the absolute temperature.

To determine the activation energy of the conduction process, we plot σ_{dc} *versus* 1000/T, as depicted in Fig. 8(a). By performing straight-line fits, we obtain three activation energies corresponding to 0.12, 0.32, and 0.68 eV, which fall within the typical range of values characteristic of semiconductors.[60]

Fig. 8(b) depicts the temperature dependency of AC conductivity at various frequencies. As the temperature inversion increases for each constant frequency, ln(σ_{ac}) decreases, displaying three linear straight lines with distinct inclinations (regions 1, 2, and 3).

The activation energies extracted from the data fit in the figure are compiled in Table 2. The trend clearly shows that E_a decreases as the frequencies increase across different temperature ranges. This phenomenon can be attributed to the rise in the applied field frequency, which amplifies the electronic transition between localized states.[61] In essence, we can assert that the mobility of charge carriers within the compound is facilitated by the hopping conduction mechanism.[62]

4.3. Impedance analysis

Fig. 9(a–c) display the impedance plot ($-Z''$ *vs.* Z') at different temperatures in the temperature ranges 313–413 K, 433–493 K and 513–673 K respectively. In all spectra, two semicircle arcs are observed. These semi-circles have a deformed shape and their centers are located below the Z' axis, which reveals that the conduction mechanism is of the non-Debye (Cole–Cole) type.[63]

The plot of the two arcs in the Nyquist diagram of KCFO, in the temperature range 313–393 K and 513–673 K, can be characterized by the response of grain boundaries and grains at low and high temperatures, respectively. The arc resulting from the impedance plot in the temperature range between 433 and 493 K described may be the effect of the grain and polarization of the electrode.

The Maxwell–Wagner equivalent circuit model is employed to fit the depressed semicircles.[64] For the three temperature

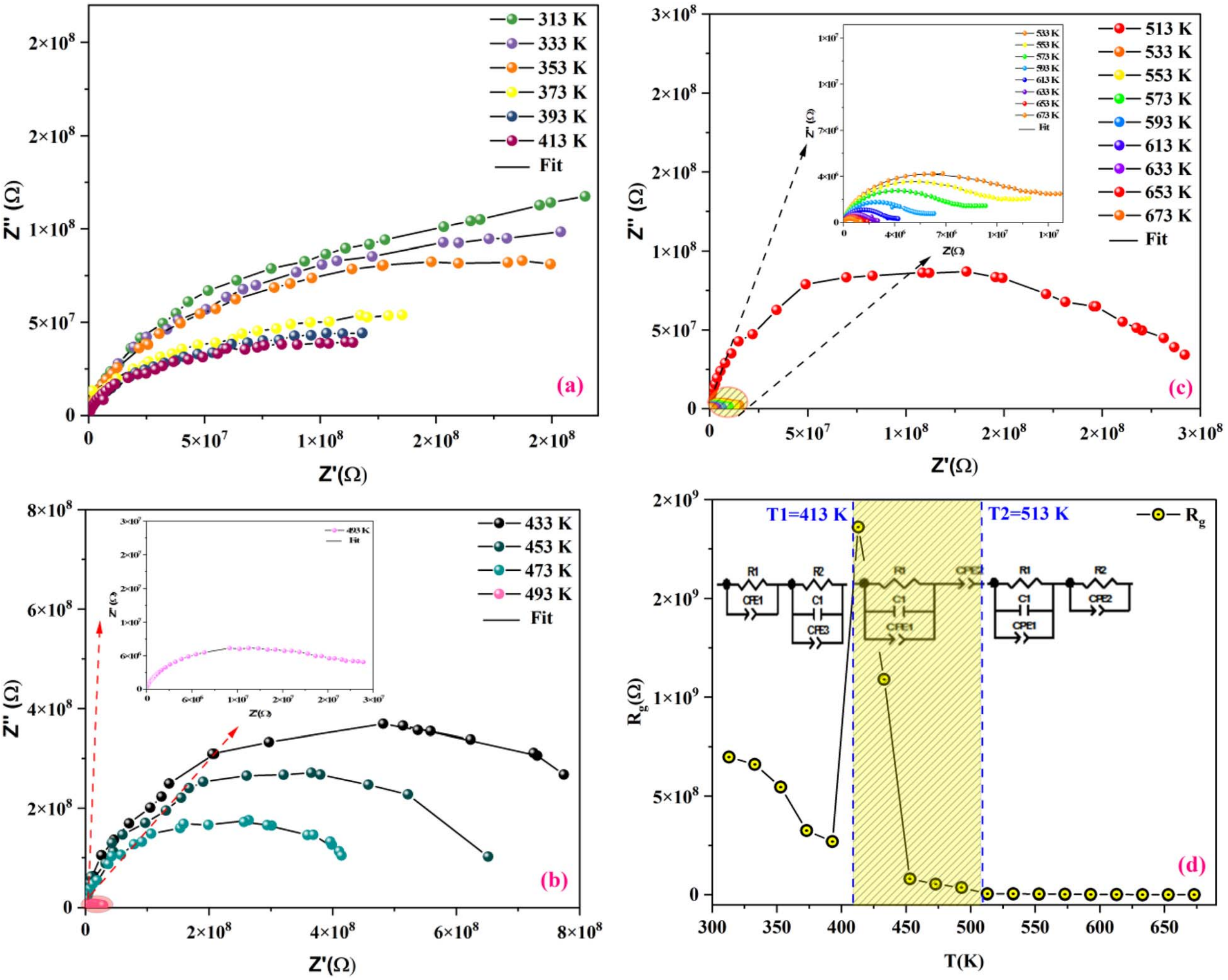

Fig. 9 Nyquist plot of MATM compound, at different temperatures, (a–c) and variation of resistance as a function of temperature (d).

regions mentioned previously, three equivalent circuit models are employed to describe the impedance spectra; two semicircular arcs are observed in Fig. 9(a) for the temperature range of 313–393 K and 513–673 K, this phenomenon is associated with grain and grain boundary effects. To derive the different electrical parameters, the experimental data are structured into an equivalent circuit comprising a series of two parallel combinations. The first combination includes a resistance (R) and a constant phase element (CPE), while the second combination comprises a parallel arrangement of resistance (R), capacitance (C), and another constant phase element (CPE).[65] Give the capacitive impedance of the CPE fractal interface (ZCPE):

$$Z_{\mathrm{CPE}} = \frac{1}{Q(j\omega)^{\alpha}} \tag{7}$$

where Q corresponds to the value of the capacitance, $j\omega$ represents a complex number where ω is the angular frequency, In the context of the model, j represents the imaginary unit, while α denotes the parameter indicating the deviation of the compressed semicircle from an ideal semicircle. When α equals 1, the element behaves as a pure capacitor, and when α equals 0, it behaves as a pure resistance. We can deduce from the equivalent electrical circuit the real part (Z') and the imaginary part (Z'') of complex impedance, which are expressed by the following equations:

$$Z' = \frac{R_{\mathrm{jg}} + R_{\mathrm{jg}}{}^{2} Q_{\mathrm{jg}} \omega^{\alpha_2} \cos\left(\frac{\alpha_2 \pi}{2}\right)}{\left(1 + R_{\mathrm{jg}} Q_2 \omega^{\alpha_2} \cos\left(\frac{\alpha_2 \pi}{2}\right)\right)^2 + \left(R_{\mathrm{jg}} Q_2 \omega^{\alpha_2} \sin\left(\frac{\alpha_2 \pi}{2}\right)\right)^2} + \frac{\frac{1}{R_{\mathrm{g}}} + Q_1 \omega^{\alpha_1} \cos\left(\frac{\alpha_1 \pi}{2}\right)}{\left(\frac{1}{R_{\mathrm{g}}} + Q_1 \omega^{\alpha_1} \cos\left(\frac{\alpha_1 \pi}{2}\right)\right)^2 + \left(C_1 \omega + Q \omega^{\alpha_1} \sin\left(\frac{\alpha_1 \pi}{2}\right)\right)^2} \tag{8}$$

$$Z'' = \frac{R_{\mathrm{jg}}{}^{2} Q_2 \omega^{\alpha_2} \sin\left(\frac{\alpha_2 \pi}{2}\right)}{\left(1 + R_{\mathrm{jg}} Q_2 \omega^{\alpha_2} \cos\left(\frac{\alpha_2 \pi}{2}\right)\right)^2 + \left(R_{\mathrm{jg}} Q_2 \omega^{\alpha_2} \sin\left(\frac{\alpha_2 \pi}{2}\right)\right)^2} + \frac{C_1 \omega + Q_1 \omega^{\alpha_1} \sin\left(\frac{\alpha_1 \pi}{2}\right)}{\left(\frac{1}{R_{\mathrm{g}}} + Q_1 \omega^{\alpha_1} \cos\left(\frac{\alpha_1 \pi}{2}\right)\right)^2 + \left(C_1 \omega + Q_1 \omega^{\alpha_1} \sin\left(\frac{\alpha_1 \pi}{2}\right)\right)^2} \tag{9}$$

From 413 K to 493 K, an equivalent circuit model can model the compound. It implies a serial association of grain resistance (R_g) associated in parallel with (CPE) and (CPE) associated in series. The corresponding circuit is deposited, as the inset Fig. 9(b) illustrates. Based on this model, we can obtain the subsequent expressions:

$$Z' = \frac{\frac{1}{R_g} + Q_1\omega^{\alpha_1}\cos\left(\frac{\alpha_1\pi}{2}\right)}{\left(\frac{1}{R_g} + Q_1\omega^{\alpha_1}\cos\left(\frac{\alpha_1\pi}{2}\right)\right)^2 + \left(C_1\omega + Q\omega^{\alpha_1}\sin\left(\frac{\alpha_1\pi}{2}\right)\right)^2} + \frac{Q_{jg}\omega^{\alpha_2}\cos\left(\frac{\alpha_2\pi}{2}\right)}{\left(Q_2\omega^{\alpha_2}\cos\left(\frac{\alpha_2\pi}{2}\right)\right)^2 + \left(Q_2\omega^{\alpha_2}\sin\left(\frac{\alpha_2\pi}{2}\right)\right)^2} \tag{10}$$

$$Z'' = \frac{C_1\omega + Q_1\omega^{\alpha_1}\sin\left(\frac{\alpha_1\pi}{2}\right)}{\left(\frac{1}{R_g} + Q_1\omega^{\alpha_1}\cos\left(\frac{\alpha_1\pi}{2}\right)\right)^2 + \left(C_1\omega + Q_1\omega^{\alpha_1}\sin\left(\frac{\alpha_1\pi}{2}\right)\right)^2} + \frac{Q_2\omega^{\alpha_2}\sin\left(\frac{\alpha_2\pi}{2}\right)}{\left(Q_2\omega^{\alpha_2}\cos\left(\frac{\alpha_2\pi}{2}\right)\right)^2 + \left(Q_2\omega^{\alpha_2}\sin\left(\frac{\alpha_2\pi}{2}\right)\right)^2} \tag{11}$$

To examine how resistances (R_g) vary with temperature, we plotted those resistances against temperature in Fig. 9(d), where it is evident that for all three temperature ranges and the temperature increase at 413 K, each resistance lowers as temperature rises. After that, the temperature drops once again; the phase transition area can account for the rise at 413 K. We notice that the values of R_g decrease if the temperature increases from 313 K to 413 K and 513 K to 673 K, which implies the semiconductor behavior. From 433 K to 493 K, the R_g values increase gradually if the temperature increases, which indicates the behavior of the metal. These values are higher than those reported in the literature, which can be explained by the potassium doping effect.[17] During this transition, depicted in Fig. 4, the KCFO undergoes a shift from the ferroelectric phase to the para-electric phase.

The analysis of M' (ω) and $-Z''$ (ω) plots allows for the determination of the movement of charge carriers and the nature of relaxation in a material, whether it is non-Debye/localized or Debye/delocalized. When impedance and modulus peaks ($M''_{\max}$ and $Z''_{\max}$) coincide at the same frequency, it indicates long-range motion. Conversely, the gap indicates a short-range motion in the conduction process. In Fig. 10, a significant mismatch between $M''_{\max}$ and $Z''_{\max}$ peaks is observed at temperatures of 373 K and 573 K. This discrepancy suggests a short-range motion of polarons within KCFO, deviating from the ideal Debye response. Notably, as the temperature rises, the shift between the peaks diminishes, leading to the deduction that the temperature increase induces the relaxation of polarons toward a delocalized state, resembling a Debye-type response within KCFO.[64]

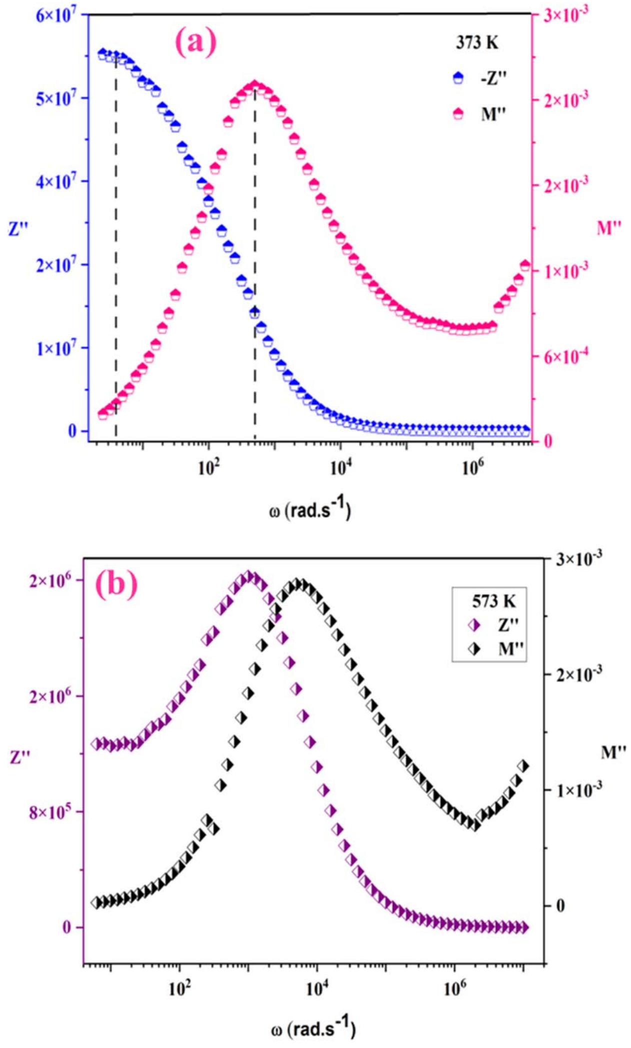

Fig. 10 $-Z''$ & M'' variation with frequency at 373 K (a) and 573 K (b).

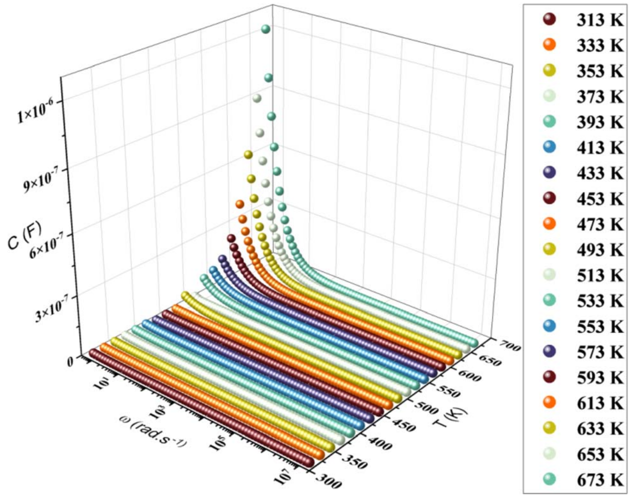

Fig. 11 Frequency dependence of capacitance spectra of KCFO.

The variation of capacitance *versus* angular frequency at different temperatures is illustrated in Fig. 11. The association between frequency and capacitance is obvious as the frequency increases, resulting in a decrease in the capacitance curve. At lower frequencies, the largest capacitance values are recorded, showing the presence of inhomogeneous barrier development at the interface induced by interface states. These interface states are capable of generating an interfacial space charge at the interface.[66,67] As previously seen in permittivity studies, the capacitance of materials decreased followed by stabilization. Furthermore, the materials predicted capacitance values at 553 K were magnitudes about 10^{-6} F. As a result, increased capacitance may improve the overall efficiency of field-effect transistor (FET) devices.

5. Conclusion

We have explored the morphology, conduction behavior, and electrical properties of the KCFO sample synthesized using the solid-state route.

XRD measurements indicate that the compound is in the orthorhombic phase of the *Pbnm* space group. Raman spectra were utilized for further examination of vibrational modes, providing confirmation of the bonding between oxygen and cations within both octahedral and tetrahedral sites. EDX analysis demonstrates the uniform distribution of iron and calcium cations. The dielectric properties confirm a phase transition from ferroelectric to paraelectric, possibly accounting for the observed anomaly in DC conductivity. The significant dielectric permittivity, robust capacitance, elevated conductivity, and minimal dielectric loss exhibited by this material underscore the potential of ferrites as valuable substances for electronic devices. A comprehensive study has been carried out on AC conductivity, complex impedance, and complex modulus across the frequency range of 10–10^6 Hz at various temperatures. The frequency-dependent AC conductivity, elucidated by Double Jonscher's law, has been investigated as a function of temperature. The conduction mechanism was analyzed employing the (CBH) model. A comprehensive analysis of the impedance data unveils the distinct contributions from both the grain and the grain boundary. In the temperature intervals 313–413 K and 513–673 K the values of the resistances *R* decrease if the temperature increases, which implies semiconductor behavior, and increase if the temperature increases from 433 to 493 K, which indicates semiconductor behavior metal.

The semiconductor nature of the material under examination suggests potential applications in optoelectronics, photodetectors, and photovoltaic. A detailed analysis of impedance data reveals contributions from both grain and grain boundaries. However, a thorough investigation into the magnetic, optical, and dielectric properties of KCFO as a function of temperature.

Conflicts of interest

The authors declare that they have no conflict of interest.

References

1 B. F. Decker and J. S. Kasper, *Acta Crystallogr.*, 1957, **10**(4), 32–337.
2 J. Cao, *et al.*, *Langmuir*, 2013, **29**(9), 3116–3124.
3 H. R. Ong, M. M. Rahman Khan, A. Yousuf, N. A. Hussain and C. K. Cheng, *RSC Adv.*, 2015, **5**(121), 100362–100368.
4 D. Hirabayashi, T. Yoshikawa, Y. Kawamoto, K. Mochizuki, and K. Suzuki, *11th International Ceramics Congress*, 2006, DOI: 10.4028/www.scientific.net/ast.45.2169.
5 Y. Matsumoto, M. Omae, K. Sugiyama and E. Sato, *J. Phys. Chem.*, 1987, **91**(3), 577–581.
6 S. Ida, K. Yamada, T. Matsunaga, H. Hagiwara, Y. Matsumoto and T. Ishihara, *Am. Chem. Soc.*, **132**(49), 17343–17345.
7 R. A. Candeia, M. I. B. Bernardi, E. Longo, I. M. G. Santos and A. G. Souza, *Mater. Lett.*, 2004, **58**(5), 569–572.
8 A. Lashtabeg and S. J. Skinner, *Mater. Chem.*, 2006, **16**(31), 3161–3170.
9 T. Hidayat, D. Shishin, S. A. Decterov and E. Jak, *Metall. Mater. Trans. B*, 2015, **47**(1), 256–281.
10 M. C. Robert, M. Thavarani, N. Pavithra, S. B. Prasath, R. Saravanan and Y. B. Kannan, *J. Supercond. Nov. Magnetism*, 2022, **35**(5), 1281–1298.
11 A. Doi, *et al.*, *J. Ceram. Soc. Jpn.*, 2014, **122**(1422), 175–178.
12 N. Sharma, K. M. Shaju, G. V. Subba Rao and B. V. R. Chowdari, *Power Sources*, 2003, **124**(1), 204–212.
13 R. A. Candeia, M. I. B. Bernardi, E. Longo, I. M. G. Santos and A. G. Souza, *Mater. Lett.*, 2004, **58**(5), 569–572.
14 Y. Matsumoto, M. Omae, K. Sugiyama and E. Sato, *Phys. Chem.*, 1987, **91**(3), 577–581.
15 S. Zouari, *et al.*, *J. Alloys Compd.*, 2008, **452**(2), 234–240.
16 K. Obata, Y. Obukuro, S. Matsushima, H. Nakamura, M. Arai and K. Kobayashi, *J. Ceram. Soc. Jpn.*, 2013, **121**(1417), 766–769.
17 L. M. Corliss, J. M. Hastings and W. Kunnmann, *Phys. Rev.*, 1967, **160**(2), 408–413.
18 H. C. Gomes, S. S. Teixeira and M. P. F. Graça, *J. Alloys Compd.*, 2022, **921**, 166026.
19 A. Manohar and C. Krishnamoorthi, *J. Alloys Compd.*, 2017, **722**, 818–827.
20 I. Petrila and F. Tudorache, *Materials*, 2021, **14**, 4916.
21 M. A. Rahman, M. T. Islam, M. S. J. Singh, M. E. H. Chowdhury and M. Samsuzzaman, *Chin. J. Phys.*, 2021, **71**, 351–364.
22 M. Sajjad, *et al.*, *Mater. Sci.: Mater. Electron.*, 2020, **31**, 21779–21791.
23 T. Tatarchuk, *et al.*, *Chemosphere*, 2021, **270**, 129414.
24 R. D. Shannon, *Acta Crystallogr., Sect. A*, 1976, **32**(5), 751–767.
25 A. Manohar and C. Krishnamoorthi, *J. Alloys Compd.*, 2017, **722**, 818–827.
26 H. C. Gomes, S. S. Teixeira and M. P. F. Graça, *J. Alloys Compd.*, 2022, **921**, 166026.
27 J. Massoudi, *et al.*, *J. Phys. Chem. C*, 2022, **126**, 2857–2867.
28 I. Soudani, K. Ben Brahim, A. Oueslati, H. Slimi, A. Aydi and K. Khirouni, *RSC Adv.*, 2022, **12**, 18697–18708.
29 I. Soudani, *et al.*, *RSC Adv.*, 2023, **13**, 9260–9272.

30 N. Singh, *et al.*, *Mater. Today: Proc.*, 2022, **65**, 2676–2682.

31 V. V. Kharton, *et al.*, *J. Electrochem. Soc.*, 2008, **155**(3), 13.

32 E. E. Ateia, S. Hussien and A. T. Mohamed, *J. Inorg. Organomet. Polym. Mater.*, 2022, **33**(1), 216–227.

33 H. Yang, S. Zhang, H. Yang, Y. Yuan and E. Li, *Ceram. Int.*, 2019, **45**(14), 16940–16947.

34 S. Attia, N. Helaili, G. Rekhila, Y. Bessekhouad and M. Trari, *Mater. Sci.: Mater. Electron.*, 2022, **33**(13), 9976–9987.

35 C. Van Caillie and R. D. Amos, *Chem. Phys. Lett.*, 2000, **328**, 446–452.

36 D. D. Miller and R. Siriwardane, *Appl. Energy*, 2018, **224**, 708.

37 N. Koleva, M. N. Ilieva, V. N. Popovb and M. Gospodinov, *Solid State Commun.*, 2003, **128**, 153–155.

38 G. Sahu, M. Das, M. Yadav, B. P. Sahoo and J. Tripathy, *Polymers*, 2020, **12**(2), 374.

39 T. Dabbebi, *et al.*, *Mater. Sci.: Mater. Electron.*, 2021, **33**(1), 490–504.

40 F. Hcini, S. Hcini, B. Alzahrani, S. Zemni and M. L. Bouazizi, *Appl. Phys. A:*, 2020, **126**, 362.

41 A. Sahoo, T. Paul, S. Maiti and R. Banerjee, *Nanotechnology*, 2022, **33**(19), 195703.

42 P. Bhuyan, D. Cho, M. Choe, S. Lee and S. Park, *Polymers*, 2022, **14**(4), 710.

43 K. C. Kao, *Dielectric Phenomena in Solids*, 2004, pp. 283–326.

44 F. Gaâbel, M. Khlifi, N. Hamdaoui, L. Beji, K. Taibi and J. Dhahri, *Mater. Sci.: Mater. Electron.*, 2019, **30**(16), 14823–14833.

45 S. Singh, G. Banappanavar and D. Kabra, *ACS Energy Lett.*, 2020, **5**(3), 728–735.

46 W. Wan, *et al.*, *Ceram. Int.*, 2018, **44**(5), 5086–5092.

47 S. Aydi, A. Amouri, S. Chkoundali and A. Aydi, *Ceram. Int.*, 2017, **43**(15), 12179–12185.

48 M. ben Abdessalem, I. Kriaa, A. Aydi and N. Abdelmoula, *Ceram. Int.*, 2018, **44**(12), 13595–13601.

49 K. Uchino and S. Nomura, *Ferroelectrics*, 1982, **44**(1), 55–61.

50 M. Smari, H. Rahmouni, N. Elghoul, I. Walha, E. Dhahri and K. Khirouni, *RSC Adv.*, 2015, **5**(3), 2177–2184.

51 K. Funke, *Solid State Ionics*, 1990, **40–41**, 200–204.

52 A. K. Jonscher, *Nature*, 1977, **267**(5613), 673–679.

53 M. Ben Bechir and A. Ben Rhaiem, *Solid State Chem.*, 2021, **296**, 122021.

54 L. Murawski, C. H. Chung and J. D. Mackenzie, *Non-Cryst. Solids*, 1979, **32**(1–3), 91–104.

55 A. A. Dakhel, *Solid-State Electron.*, 2005, **49**(12), 1996–2001.

56 R. H. Chen, R. Y. Chang and S. C. Shern, *Phys. Chem. Solids*, 2002, **63**(11), 2069–2077.

57 S. R. Elliott, *Adv. Phys.*, 1987, **36**(2), 135–217.

58 R. Punia, R. S. Kundu, M. Dult, S. Murugavel and N. Kishore, *Appl. Phys.*, 2012, **112**(8), 083701.

59 A. R. Long, *Adv. Phys.*, 1982, **31**(5), 553–637.

60 M. Ajili, A. Oueslati, M. B. Gzaiel and M. Gargouri, Investigation of optical and transport properties of the semiconducting α-KYP_2O_7 compound, *Opt. Quantum Electron.*, 2021, **53**, 209.

61 M. Okutan, E. Basaran, H. I. Bakan and F. Yakuphanoglu, *Phys. B Condens. Matter*, 2005, **364**, 300–305.

62 H. Zhang, A. Chang and C. Peng, *Microelectron. Eng.*, 2011, **88**(9), 2934–2940.

63 A. Singh, R. Chatterjee, S. K. Mishra, P. S. R. Krishna and S. L. Chaplot, *Appl. Phys.*, 2012, **111**(1), 014113.

64 P. Córdoba-Torres, T. J. Mesquita, O. Devos, B. Tribollet, V. Roche and R. P. Nogueira, *Electrochim. Acta*, 2012, **72**, 172–178.

65 R. Bergman, *J. Appl. Phys.*, 2000, **88**(3), 1356–1365.

66 G. R. Neupane, M. Bamidele, V. Yeddu, D. Y. Kim and P. Hari, *Mater. Res.*, 2022, **37**(7), 1357–1372.

67 H. H. Gullu and D. E. Yildiz, *Mater. Sci.: Mater. Electron.*, 2021, **32**(10), 13549–13567.